Chemical Science

Accepted Manuscript

This article can be cited before page numbers have been issued, to do this please use: H. Gao, X. He, J. Li, Q. Zhu, C. Qin, L. Sun, S. Zhi, L. Yang, W. Zhan, J. Zhao and X. Han, *Chem. Sci.*, 2025, DOI: 10.1039/D5SC05362E.

ROYAL SOCIETY OF CHEMISTRY

rsc.li/chemical-science

View Article Online
DOI: 10.1039/D5SC05362E

ARTICLE

Constructing a Visible-Light-Excited Z-scheme Heterojunction by Engineering the Directional N-C/Cu Insertion layer: Overcoming the Work Function Mismatches

Received 00th January 20xx,
Accepted 00th January 20xx

DOI: 10.1039/x0xx00000x

Hao Gao,[†a] Xiaoxiao He,[†b] Jinbu Li,[†a] Qiang Zhu,[a] Chengyu Qin,[a] Liming Sun,*[a] Shuting Zhi,[a] Lei Yang,[c] Wenwen Zhan,*[a] Jianwei Zhao,[c] and Xiguang Han*[a]

The construction of S-scheme heterojunctions is constrained by stringent work function (Φ) matching between oxidation and reduction photocatalysts, which limits material selection. Here, we present an innovative interfacial engineering strategy to overcome Φ-mismatched barriers by introducing a nitrogen-doped carbon (N-C) mediator and Cu nanoparticles at the WO_3/Cu_2O interface. Through a "post-deposition and pyrolysis" approach, we fabricated a tightly integrated Z-scheme WO_3/N-C/Cu/Cu_2O heterojunction, where the N-C layer and metallic Cu synergistically redirect photogenerated carrier recombination, preserving the high redox potentials of WO_3 (VB: +2.62 V) and Cu_2O (CB: −1.41 V). Femtosecond transient absorption spectroscopy and electron paramagnetic resonance data revealed that interfacial electrons from WO_3 transferred to N-C and recombined with holes originated from Cu_2O on Cu via the directional N-C/Cu insertion layer. The optimized heterojunction exhibits exceptional photocatalytic performance under blue light (450 nm), achieving a 99% yield in homo-coupling of terminal alkyne to 1,3-conjugated diynes and a hydrogen evolution rate 300-fold higher than that of conventional WO_3/Cu_2O. This work provides a universal paradigm for designing Z-scheme systems with mismatched components, unlocking new possibilities for solar energy conversion and organic synthesis.

Introduction

Photocatalytic systems, which harness solar energy to drive redox reactions, hold immense potential for sustainable energy conversion and organic synthesis.[1-5] However, their efficiency is fundamentally limited by rapid charge recombination and inadequate redox potentials.[6,7] Heterojunction photocatalysts, particularly step-scheme (S-scheme) systems, have emerged as a promising strategy to enhance charge separation while preserving strong redox capabilities (Scheme 1).[8-17] In S-scheme heterojunctions, the band bending, a built-in electric field and Coulombic attraction at the interface between oxidation (OP) and reduction photocatalysts (RP) promote selective recombination of low-energy carriers, retaining high-energy electrons and holes for surface reactions.[18-25] However, the construction of S-scheme heterojunctions for photocatalytic applications encounters two primary challenges. Firstly, optimizing the bandgaps is critical. To facilitate the step-scheme migration of photogenerated carriers in S-scheme heterojunctions, both components must be simultaneously photo-excited.[26,27] However, selecting narrow-bandgap semiconductors to ensure a visible light response may compromise the overall redox capability of the S-scheme heterojunction photocatalytic system. Secondly, work function (Φ) matching between components is essential.[28-30] The formation of an S-scheme heterojunction mandates that the work function of the RP is lower than that of the OP ($\Phi_{RP}<\Phi_{OP}$). These challenges severely limit material selection and often exclude semiconductors with superior light absorption or catalytic activity.

WO_3 and Cu_2O, as visible-light-responsive OP and RP candidates, exemplify this dilemma and have been excluded as the candidates for S-scheme heterojunction.[31-33] WO_3 possesses a highly positive valence band ideal for oxidation;[34-40] while Cu_2O offers a negative conduction band suitable for reduction.[41-44] However, their intrinsic work function mismatch ($\Phi_{WO3} < \Phi_{Cu2O}$) leads to the formation of undesired II-type heterojunction other than S-scheme heterojunction, where electrons accumulate in CB of WO_3 and holes in VB of Cu_2O, drastically diminishing their redox potentials. Previous attempts to address this challenge, such as doping or morphology tuning, have failed to reconcile interfacial energetics with efficient charge dynamics, leaving the core issue of Φ-mismatch unresolved.

Herein, we propose an interfacial engineering strategy to override the work function limitation by introducing a nitrogen-doped carbon (N-C) mediator and metallic Cu nanoparticles at the WO_3/Cu_2O interface. The N-C layer, with a low Φ, creates a directional electron transfer pathway from N-C to WO_3, while Cu nanoparticles act as hole reservoirs for Cu_2O, collectively

[a] Jiangsu Key Laboratory of Green Synthetic Chemistry for Functional Materials, Department of Chemistry, School of Chemistry & Materials Science, Jiangsu Normal University, Xuzhou, 221116, P. R. China.
[b] State Key Laboratory of Precision Spectroscopy, East China Normal University, Shanghai, 200241, P. R. China.
[c] Shenzhen HUASUAN Technology Co., Ltd, Shenzhen, 518055, P. R. China.
† These authors contributed equally.
Supplementary Information available. See DOI: 10.1039/x0xx00000x

reshaping the built-in electric field to form a Z-scheme heterojunction. Through a "post-deposition and pyrolysis" synthetic approach, we constructed a tightly integrated WO_3/N-C/Cu/Cu_2O heterojunction, where transient absorption and in-situ electron paramagnetic resonance data confirm that photogenerated electrons from WO_3 transfer to N-C and recombine with holes from Cu_2O on Cu nanoparticles via the N-C/Cu interface, preserving the high-energy carriers for redox reactions. The optimized system achieves a 99% yield in terminal alkyne homo-coupling and a hydrogen evolution rate 300-fold higher than conventional WO_3/Cu_2O under the illumination of blue light LED. This work not only resolves the long-standing Φ-mismatch challenge but also establishes a universal interfacial engineering paradigm for constructing Z-scheme systems from incompatible components. By decoupling material selection from intrinsic electronic constraints, our strategy opens new avenues for developing high-performance photocatalysts tailored for solar fuel production and organic transformations.

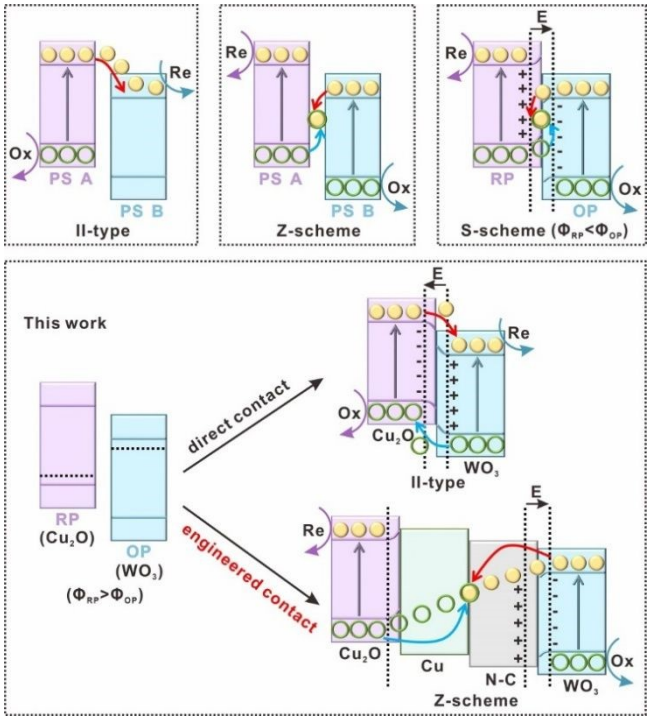

Scheme 1. The schematic diagram of the migration and separation pathways of photogenerated carriers in II-type, Z-scheme, and S-scheme heterojunctions, as well as the heterojunctions developed in this work.

Results and discussion

The synthesis procedure of mesoporous WO_3/N-C/Cu/Cu_2O cuboctahedra via the “post-deposition and pyrolysis” method is schematically illustrated in Fig. 1a. Firstly, well-defined HKUST-1 with a cuboctahedral structure was synthesized through a simple solvothermal reaction, utilizing copper nitrate trihydrate ($Cu(NO_3)_2{\cdot}3H_2O$) as metal salt, 1,3,5-benzenetricarboxylic acid as organic ligand, and benzimidazole as the modulator. For detailed experimental procedures, please refer to the ESI. Then, the obtained HKUST-1 precursor and monoclinic WO_3 (the relevant preparation and characterization details are presented in ESI and Fig. S1) were uniformly immersed in methanol. Subsequently, the mixture was heated at 120 °C for 6 hours. During this treatment, the cuboctahedra WO_3/HKUST-1 precursor could be obtained. Afterward, a pyrolysis treatment was carried out at 300 ℃ in an Ar atmosphere, and Cu^{2+} ions within the WO_3/HKUST-1 precursor were transformed into Cu_2O and metallic Cu. Simultaneously, benzimidazole and 1,3,5-benzenetricarboxylic acid underwent in-situ carbonization to form an external nitrogen-doped carbon (N-C) layer. As a result, the WO_3/HKUST-1 precursor evolved into mesoporous cuboctahedral WO_3/N-C/Cu/Cu_2O.

The composite and structure of the products obtained at different stages were characterized by powder X-ray diffraction (XRD) and field-emission scanning electron microscopy (FE-SEM). The XRD pattern of HKUST-1 precursor is shown in Fig. S2. The precursor exhibits sharp diffraction peaks in good agreement with the simulated pattern of HKUST-1 with high crystallinity.[45] The FE-SEM image (Fig. 1b) illustrates that the prepared HKUST-1 precursor possesses a cuboctahedral morphology characterized by high uniformity and smooth surface. After the deposition of WO_3, the resulting products (Fig. 1c) maintain a uniform cuboctahedral structure with excellent monodispersity, and their surfaces are decorated with small particles. As revealed by XRD analysis (Fig. S3a), the diffraction peaks are well consistent with monoclinic WO_3 phase (PDF no. 01-072-1465) and simulated HKUST-1 pattern, thereby confirming the coexistence of WO_3 and HKUST-1 in the composite sample WO_3/HKUST-1. The simultaneous presence of Cu, W, O, C and N elements in WO_3/HKUST-1 was revealed by the energy-dispersive X-ray spectroscopy (EDX) elemental mapping (Fig. S3b-h). After annealing treatment in an Ar atmosphere, the WO_3/HKUST-1 phase transformed into WO_3/N-C/Cu/Cu_2O. The XRD pattern shown in Fig. S4 demonstrates a good match between the diffraction peaks of the annealed product and monoclinic WO_3 (PDF no. 01-072-1465), cubic Cu_2O (PDF no. 01-077-0199), and cubic Cu (PDF no. 00-004-0836). Raman spectrum of WO_3/N-C/Cu/Cu_2O (Fig. S5) shows a D-band peak at 1344 cm^{-1} and a G-band peak at 1562 cm^{-1}, which are related with the defected graphic carbon. These results provide strong evidence for the successful phase transformation to WO_3/N-C/Cu/Cu_2O. The WO_3/N-C/Cu/Cu_2O composite have maintained the cuboctahedral morphology of WO_3/HKUST-1 precursor, but underwent a structural change from a solid to a hollow configuration, as depicted in Fig. 1d. The porosity of the obtained WO_3/N-C/Cu/Cu_2O composite was characterized using nitrogen adsorption-desorption isotherms (Fig. S6). The Barrett-Joyner-Halenda (BJH) pore sizes distribution has been determined to be approximately 19 nm, and the Brunauer Emmett Teller (BET) surface area of WO_3/N-C/Cu/Cu_2O has been measured to be around 61.6 m^2/g.

The structural and component information of WO_3/N-C/Cu/Cu_2O was comprehensively investigated using transmission electron microscopy (TEM). The TEM image (Fig. 1e) reveals that the synthesized WO_3/N-C/Cu/Cu_2O exhibits a hollow cuboctahedral morphology, accompanied by dispersed

small particles. The magnified TEM image (Fig. 1f) clearly reveals the presence of a well-defined heterojunction interface between the dispersed particles and the amorphous carbon layers. The HRTEM (high-resolution TEM) image of the marked yellow zone of the dispersed particle in Fig. 1f is depicted in Fig. 1g. The lattice spacing of 0.365 nm can be ascribed to the (200) plane of the monoclinic WO_3 phase, thereby indicating that the dispersed particle is a WO_3 particle. The magnified TEM image (Fig. 1h, red zone in Fig. 1e) indicates that the shell structure of the hollow cuboctahedra is assembled by nanoparticles. The HRTEM image of zone 1 in Fig. 1h (Fig. 1i) exhibits a lattice spacing of 0.208 nm, corresponding to the (111) plane of cubic Cu phase. The HRTEM image of zone 2 in Fig. 1h (Fig. 1j) displays a lattice spacing of 0.212 nm, which can be attributed to the (200) plane of cubic Cu_2O phase. The presence of the Cu/Cu_2O heterojunction interface can be confirmed by these findings. The high-angle annular dark-field scanning transmission electron microscope (HAADF-STEM) images in Fig. 1k further verify the existence of a hollow structure with small particles on the surfaces. The energy-dispersive X-ray spectroscopy (EDX) mapping (Fig. 1l-p) reveals a homogeneous distribution of Cu, W, O, C, and N elements within the cuboctahedral framework. The combination of XRD, HRTEM, and EDX analyses provides robust evidence for the successful synthesis of hollow cuboctahedra featuring a WO_3/N-C/Cu/Cu_2O interface.

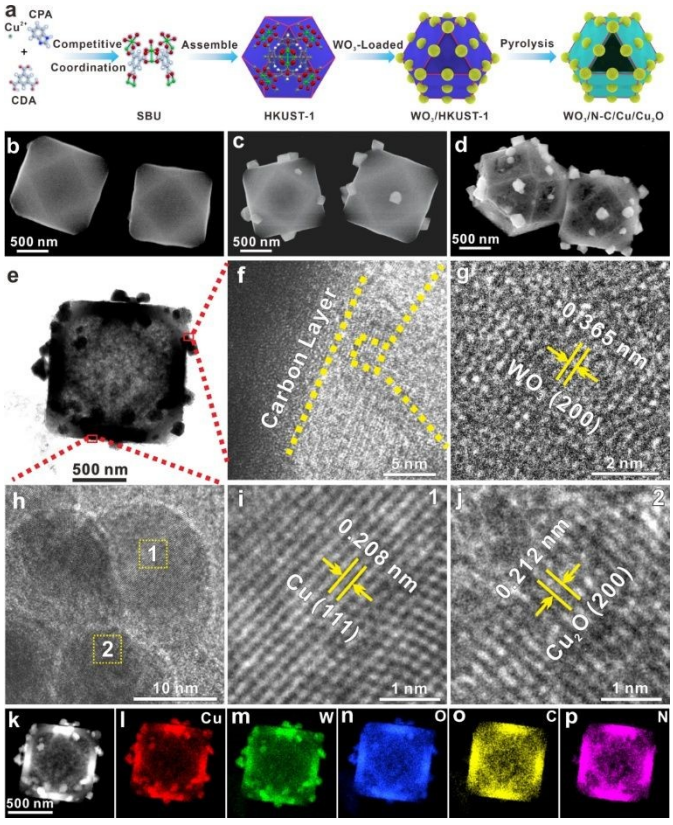

Fig. 1 (a) Schematic showing the synthetic process of WO_3/N-C/Cu/Cu_2O, FE-SEM images of (b) cuboctahedra HKUST-1 precursor, (c) cuboctahedra WO_3/HKUST-1 precursor, (d) WO_3/N-C/Cu/Cu_2O, (e) TEM image of WO_3/N-C/Cu/Cu_2O, (f) the magnified TEM image of marked area in Fig. 1e, (g) the corresponding HRTEM of marked area in Fig. 1f, (h) the magnified TEM image of marked area in Fig. 1e, (i, j) the corresponding HRTEM images of area 1 and 2 in Fig. 1h, (k) STEM image of WO_3/N-C/Cu/Cu_2O, (l-p) EDX elemental mapping of Cu, W, O, C and N elements.

The synthesized WO_3/N-C/Cu/Cu_2O heterojunctions were further analyzed using X-ray photoelectron spectroscopy (XPS) to determine the chemical states and static electron transfer between heterojunctions (Fig. S7 and Fig. 2a-d). To explore the electronic interactions among the components of the WO_3/N-C/Cu/Cu_2O heterojunction, WO_3/Cu_2O (details in ESI and Fig. S8), N-C/Cu/Cu_2O (details in ESI and Fig. S9), WO_3, and Cu_2O (details in ESI and Fig. S10) were employed as reference samples. As illustrated in Fig. 2a, the characteristic peaks located at 35.5 eV and 37.7 eV in the W 4f XPS spectrum of pristine WO_3 are attributed to the W $4f_{7/2}$ and W $4f_{5/2}$ of W^{6+}, respectively.[46] Compared with pristine WO_3, the W 4f peaks of the WO_3/N-C/Cu/Cu_2O heterojunction have shifted to a lower energy region, indicating that WO_3 in this heterojunction is in an electron-acquiring state. In contrast, WO_3 in WO_3/Cu_2O heterojunction is in the opposite state since the W 4f peaks have shifted to a higher energy region relative to pristine WO_3. In Fig. 2b, the peaks at binding energies of 932.8 eV and 952.6 eV are assigned to Cu $2p_{3/2}$ and Cu $2p_{1/2}$ of Cu^+/Cu^0 in the N-C/Cu/Cu_2O heterojunction, respectively. Meanwhile, the remaining peaks (934.8 eV and 954.7 eV) can be assigned to Cu^{2+}, which is due to the surface oxidation of Cu^+ ions and Cu^0. In comparison with N-C/Cu/Cu_2O, the Cu 2p peaks in the WO_3/N-C/Cu/Cu_2O heterojunction shift towards a higher energy region. Combining with the previous analysis of the W 4f XPS spectra, this shift indicates that the directed transfer of interfacial electrons to WO_3 from N-C/Cu/Cu_2O during the formation of the WO_3/N-C/Cu/Cu_2O heterojunctions. While, Fig. 2c indicates that the characteristic peaks of Cu^+ in the WO_3/Cu_2O heterojunction shift towards a lower binding energy, and no characteristic peaks of Cu^{2+} are detected. This observation indicates that in WO_3/Cu_2O heterojunction, interfacial electrons transfer from WO_3 to Cu_2O, supported by the above analysis of the W 4f XPS spectra. Fig. 2d presents the XPS spectra of C 1s, N 1s, and O 1s in the WO_3/N-C/Cu/Cu_2O heterojunction. In the C 1s XPS spectra, the peak at 284.8 eV corresponds to alkyl-C bonds, the peak at 286.1 eV is associated with sp^2-carbon containing nitrogen atoms (C-N bonds), and the peak at 288.7 eV is assigned to carbon atoms bonded to carbonyl groups (C=O). The N 1s peak at 399.6 eV can be attributed to graphene-N, further confirming N doping within the carbon layer. The high-resolution O 1s spectrum can be deconvoluted into three major peaks centered at 530.7 eV, 532.0 eV, and 533.6 eV, corresponding to lattice oxygen (O_L), oxygen-deficient regions (O_V), and dissociated and chemisorbed oxygen (O_C), respectively. The analysis of XPS spectra not only clarify the chemical states and elemental compositions within the synthesized WO_3/N-C/Cu/Cu_2O heterojunction but also indicate an interesting phenomenon, i.e., the direction of interfacial electron migration is opposite in WO_3/N-C/Cu/Cu_2O and WO_3/Cu_2O heterojunctions.

To investigate the reason for the opposite direction of interfacial electron migration, we calculated the work functions (Φ) of WO_3, N-C layer, Cu_2O, and Cu, since work function is a

critical parameter for understanding interfacial charge transfer mechanisms.[47] As shown in Fig. 2e-h, the work functions of WO_3, N-C layer, Cu_2O, and Cu have been calculated to be 4.54 eV, 3.55 eV, 4.71eV, and 4.69 eV, respectively. The work function of WO_3 is lower than Cu_2O, which facilitates the migration of interfacial electrons from WO_3 to Cu_2O when forming WO_3/Cu_2O heterojunction upon direct contact. Consequently, an internal electric field directed from Cu_2O to WO_3 is established at the WO_3/Cu_2O interface. In contrast, when WO_3 is in direct contact with the N-C layer, the lower work function of the N-C layer than WO_3 leads to the electron transfer from N-C layer to WO_3 at the interface, resulting in a built-in electric field oriented from the N-C layer toward WO_3. The differences in work functions among WO_3, the N-C layer, and Cu_2O offer a reasonable explanation for the opposing directions of interfacial electron migration observed during the formation of the WO_3/N-C/Cu/Cu_2O and WO_3/Cu_2O heterojunctions. The distinct directions of electron migration at these interfaces results in oppositely oriented built-in electric fields, which underpin the II-type transfer mechanism of photogenerated carriers in the WO_3/Cu_2O heterojunction and the Z-scheme transfer mechanism of photogenerated carriers in the WO_3/N-C/Cu/Cu_2O heterojunction.

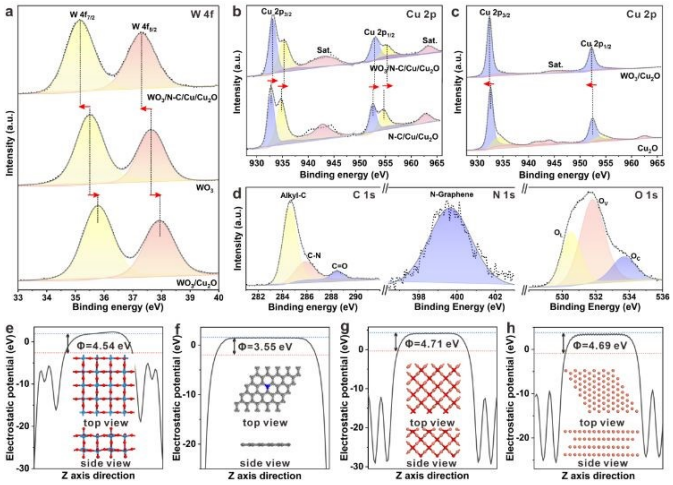

Fig. 2 (a) W 4f XPS of WO_3/N-C/Cu/Cu_2O, N-C/Cu/Cu_2O and WO_3, (b) Cu 2p XPS of WO_3/N-C/Cu/Cu_2O and N-C/Cu/Cu_2O, (c) Cu 2p XPS of WO_3/Cu_2O and Cu_2O, (d) C 1s, N 1s, and O 1s XPS of WO_3/N-C/Cu/Cu_2O. The electrostatic potentials and corresponding models of (e) WO_3, (f) N-C, (g) Cu_2O and (h) Cu. The red, light blue, grey, blue, and orange spheres represent O, W, C, N, and Cu atoms, respectively. Blue and red dashed lines indicate the vacuum and Fermi energy levels.

UV-vis diffuse reflectance spectra and valence band XPS spectra (VB-XPS) have been measured to investigate the optical properties and the band positions of the catalysts. As shown in Fig. S11a, the optical absorption edges of pristine WO_3 and Cu_2O fall within the visible light spectrum, thereby endowing the WO_3/N-C/Cu/Cu_2O heterojunction with excellent light response property in this region. The intrinsic band gap values (E_g) of pristine WO_3 and Cu_2O are estimated to be 2.54 eV and 1.82 eV, respectively (Fig. S11b). The valence band potential (E_{VB}) can be evaluated by VB-XPS spectra. According to Fig. S11c, the E_{VB} values of pristine WO_3 and Cu_2O are measured to be 2.62 V and 0.41 V (vs. NHE), respectively. The conduction band potential (E_{CB}) can be calculated using the equation of $E_g=E_{VB}-E_{CB}$.[57] Therefore, the E_{CB} values for WO_3 and Cu_2O are estimated to be 0.08 V and -1.41 V (vs. NHE), respectively.

Electron paramagnetic resonance (EPR) measurements have also been conducted to systematically study the mechanisms of charge separation and transfer in WO_3/N-C/Cu/Cu_2O heterojunction. Superoxide ($\cdot O_2^-$) and hydroxyl (·OH) radicals can be trapped by 5,5-dimethyl-1-pyrroline N-oxide (DMPO), a well-established spin-trapping agent, and subsequently detected through EPR spectroscopy. As illustrated in Fig. 3a and c, no signal can be detected under dark condition. Under 15 min of blue LED irradiation, the characteristic peaks of DMPO-$\cdot O_2^-$ and DMPO-·OH have been detected in the WO_3/N-C/Cu/Cu_2O heterojunction, while no such signals can be detected in the WO_3/Cu_2O heterojunction. Based on the aforementioned information, it is evident that the CB position of Cu_2O is more negative than the $O_2/\cdot O_2^-$ potential (-0.33 V vs. NHE), while the VB position of WO_3 is more positive than the $H_2O/\cdot OH$ potential (2.38 V vs. NHE). In contrast, the CB position of WO_3 is more positive than the $O_2/\cdot O_2^-$ potential, and the VB potential of Cu_2O is more negative than the $H_2O/\cdot OH$ potential. Therefore, the simultaneous generation of $\cdot O_2^-$ and ·OH under light irradiation indicates that when WO_3/N-C/Cu/Cu_2O heterojunction as the catalyst to participate the reaction, the photogenerated electrons are ultimately enriched in the CB of Cu_2O, while the photogenerated holes are accumulated in the VB of WO_3. This provides strong evidence for the Z-scheme transfer mechanism in the WO_3/N-C/Cu/Cu_2O heterojunction. Neither $\cdot O_2^-$ nor ·OH is produced in WO_3/Cu_2O under light irradiation, consistent with the II-type charge transfer mechanism in WO_3/Cu_2O heterojunction. In addition, as exhibited in Fig. 3b and d, the peak intensities of $\cdot O_2^-$ and ·OH radicals in WO_3/N-C/Cu/Cu_2O gradually increases with prolonged in-situ irradiation time. This indicates that the Z-scheme structure facilitates efficient separation and transfer of photogenerated carriers, thereby promoting the generation of more active radical species. The above results from EPR and XPS confirm that inserting the N-C layer and Cu into the interfaces of WO_3/Cu_2O heterojunction enables the formation of a Z-scheme WO_3/N-C/Cu/Cu_2O heterojunction.

The Z-scheme transfer mechanism of photogenerated carriers in WO_3/N-C/Cu/Cu_2O heterojunction under light illumination is further illustrated in Fig. 3e. When all the catalysts (WO_3, N-C layer, Cu, and Cu_2O) are in contact, three distinct interfaces are formed. Given that the N-C layer has a lower work function than WO_3, electrons spontaneously transfer from the N-C layer to WO_3 until the Fermi level at the interface reach equilibrium. This electron redistribution at the WO_3/N-C interface results in band bending and a build-in internal electric field near the interface. Due to the similar work functions of Cu and Cu_2O, they can form an ohmic contact directly. Upon illumination, WO_3 and Cu_2O become excited and generate electron-hole pairs. Under the influence of the internal electric field and band bending, the photogenerated electrons from the CB of WO_3 are driven towards the N-C layer. Due to the ohmic contact and the p-type characteristic of Cu_2O, the photogenerated holes from the VB of Cu_2O transfer to Cu

View Article Online
DOI: 10.1039/D5SC05362F

while simultaneously consuming photogenerated electrons on the N-C layer. Consequently, the oxidation-type photocatalyst of WO_3 forms hole-rich regions, whereas the reduction-type photocatalyst of Cu_2O forms electron-rich regions. This process effectively enhances the transport of photogenerated charge carriers and maintains the high redox capability in the WO_3/N-C/Cu/Cu_2O heterojunction.

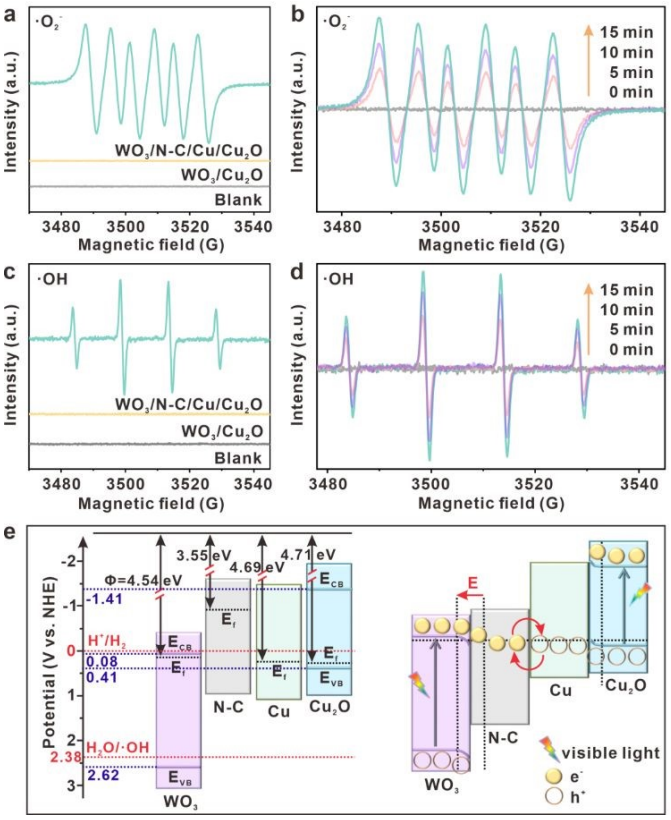

Fig. 3 EPR spectra of DMPO-·O_2^- (a) in the presence of WO_3/N-C/Cu/Cu_2O and WO_3/Cu_2O heterojunctions upon irradiation with blue LEDs for 15 min and (b) in the presence of WO_3/N-C/Cu/Cu_2O upon irradiation with blue LEDs for 0, 5, 10 and 15 min. EPR spectra of DMPO-·OH (c) in the presence of WO_3/N-C/Cu/Cu_2O and WO_3/Cu_2O heterojunctions upon irradiation with blue LEDs for 15 min and (d) in the presence of WO_3/N-C/Cu/Cu_2O upon irradiation with blue LEDs for 0, 5, 10 and 15 min. (e) The Z-scheme charge transfer mechanism in WO_3/N-C/Cu/Cu_2O under visible light irradiation.

The charge transfer dynamics of the Z-scheme WO_3/N-C/Cu/Cu_2O heterojunction has been investigated by femtosecond transient absorption (fs-TA) spectroscopy. As shown in Fig. 4a, pristine WO_3 exhibits a pronounced excited-state absorption (ESA) signal (ΔA>0) at 750 nm. According to previous research reports,[58] this signal is attributed to defect-trapped electrons. Notably, after constructing the WO_3/N-C/Cu/Cu_2O heterojunction, the ESA signal at 750 nm completely has vanished and is replaced by ground-state bleaching (GSB, ΔA<0) signal. This signal inversion demonstrates that interfacial charge transfer efficiently quenches defect-trapped electrons in WO_3. Combined with the energy structure analysis (Fig. 3e), it is evident that the conduction band (CB) electrons of WO_3 preferentially recombine with the valence band (VB) holes of Cu_2O through the N-C/Cu interfacial pathway, mediated by the N-C layer. This process blocks the accumulation of defect-state electrons in WO_3, thereby preserving the excited-state electrons in the CB of Cu_2O for prolonged activation (>1 μs). These results corroborate our prior detection of long-lived GSB signals in Cu_2O-carbon composites when illuminated under near-infrared irradiation.[50]

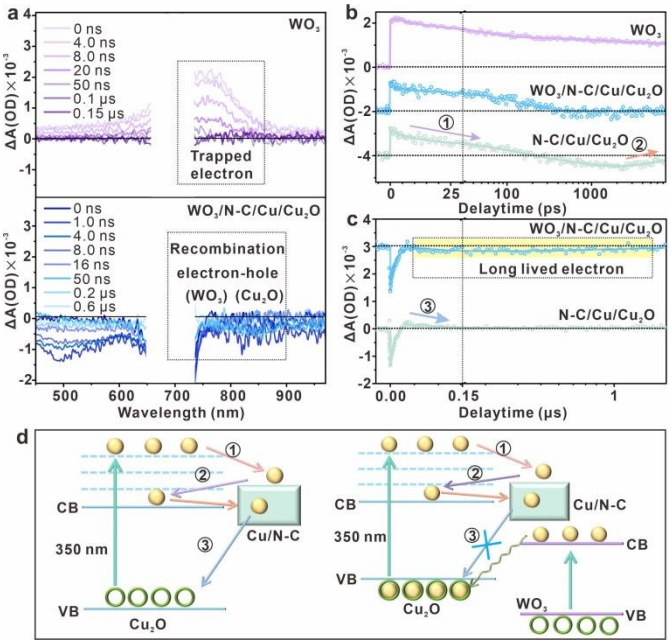

Fig. 4 (a) Transient absorption spectra of WO_3/N-C/Cu/Cu_2O and WO_3. (b, c) Kinetics of WO_3/N-C/Cu/Cu_2O, N-C/Cu/Cu_2O and Cu_2O at 750 nm. (d) Schematic diagram of charge migration paths in N-C/Cu/Cu_2O and WO_3/N-C/Cu/Cu_2O.

Fig. 4b and c show the kinetic curves at 750 nm and the data are fitted using multi-exponential decay components, as listed in Table S1 and S2. For pristine WO_3, a fast ESA decay (τ_1=36 ps) has been provided, consistent with shallow defect electron trapping at surface defect states. Then the excited electron was trapped by deep-defect states with a time constant of about 37 ns. In contrast, the kinetic curve of N-C/Cu/Cu_2O was fitted by a multiexponential function with a non-decay offset. The optimal fit reveals two decay components: a fast one with a time constant of 6.0 ps and a slow one of 97 ps. The fast decay process is assigned to the trapping of holes in surface defects, while the 97 ps time constant should reflect the movement of electrons to deep-trapped states (process 1 in Fig. 4d). The 1.1 ns time constant reflects carrier de-trapping, which drives the formation of GBS (process 2 in Fig. 4d). The GSB recovers within 18 ns and is followed by an ESA signal with a time constant of 48 ns (process 3 in Fig. 4d). Notably, the heterojunction (WO_3/N-C/Cu/Cu_2O) displays accelerated decay processes with the time constant of 2.6 ps and slow 153 ps. The absence of de-trapping process in WO_3/N-C/Cu/Cu_2O suggests interfacial charge transfer from WO_3 to Cu_2O. Then, the kinetic behavior of the heterojunction demonstrates a dual-phase evolution: GSB recovery (Table S2, τ_1=3.0 ns, τ_2=19 ns) followed by an ESA (τ_3=36 ns) signal, evidencing defect-engineered carrier lifetime extension via N-doped carbon layer. Remarkably, the WO_3/N-C/Cu/Cu_2O heterojunction shows unique behavior: following the initial GSB recovery, a secondary bleach feature grows

View Article Online DOI: 10.1039/D5SC05761E

stronger, with carrier lifetimes surpassing 1 μs. This divergence originates from the rapid interfacial recombination of conduction band (CB) electrons in WO_3 with valence band (VB) holes in Cu_2O at the heterojunction interface (Fig. 3e), thereby suppressing the charge transfer pathway (process 3) observed in N-C/Cu/Cu_2O. Consequently, the CB electrons in Cu_2O remain energetically active, significantly enhancing catalytic performance through interfacial carrier engineering.

To explore the role of the WO_3/N-C/Cu/Cu_2O interface in photocatalytic performance, a series of heterojunctions with various W-to-Cu molar ratios have been synthesized. The samples labelled as C/Cu, W/C/Cu-1, W/C/Cu-2. W/C/Cu-3, and W/C/Cu-4 represent the WO_3/N-C/Cu/Cu_2O heterojunctions with W-to-Cu molar ratio of 0, 1:3, 1:2, 2:3, and 3:4, respectively. As shown in the SEM images in Fig. 5a, as the W-to-Cu molar ratio increases, the density of WO_3 particles deposited on the surface of the N-C/Cu/Cu_2O cuboctahedra rises significantly. The homo-coupling reaction of phenylacetylene to 1,4-Diphenylbutadiyne has been chosen as the target reaction (Fig. S12). As illustrated in Fig. 5a and b, the deposition of WO_3 to form a WO_3/N-C/Cu/Cu_2O interface enhances the photocatalytic activity of N-C/Cu/Cu_2O. The photocatalytic performance of the WO_3/N-C/Cu/Cu_2O heterojunction improves with the addition of WO_3 until the W-to-Cu molar ratio reaching 3:4. Specifically, the photocatalytic activity of W/C/Cu-4 is lower than W/C/Cu-3. This decrease is mainly attributed to the excessive loading of WO_3, which obstructs the photoexcitation of Cu_2O and disrupts the smooth operation of the Z-scheme photogenerated carrier migration mechanism. Fig. 5c illustrates the comparative photocatalytic activities of WO_3/N-C/Cu/Cu_2O (with a W-to-Cu molar ratio of 2:3), N-C/Cu/Cu_2O, WO_3/Cu_2O, Cu_2O, and WO_3 in the terminal alkyne homo-coupling reaction. The results indicate that the photocatalytic activity follows the order: WO_3/N-C/Cu/Cu_2O > N-C/Cu/Cu_2O > WO_3/Cu_2O > Cu_2O > WO_3. Based on the reaction mechanism of terminal alkyne homo-coupling,[51-56] pristine WO_3 cannot generate the crucial Cu(I)-related intermediates and therefore exhibits no catalytic activity for this reaction. The catalytic performance of N-C/Cu/Cu_2O and WO_3/Cu_2O heterojunctions surpasses pristine Cu_2O due to the directional charge transfer at the heterojunction interface, which facilitates the conversion of Cu(I)-related species into electron-deficient Cu(II)-related species. This conversion enables the dissociation of Cu(II)-related species, leading to the formation of C_{sp}-C_{sp} homo-coupling products.[48] Furthermore, the photocatalytic efficiency of the WO_3/N-C/Cu/Cu_2O heterojunction is significantly enhanced compared to N-C/Cu/Cu_2O and WO_3/Cu_2O. It benefits from both the internal charge rearrangement within the Cu(I)-related species and the generation of $\cdot O_2^-$, which further promotes the transformation into Cu(II)-related species. Since there is no obvious relationship between the surface area and the activity (Fig. S13), the significantly enhanced photocatalytic activity of WO_3/N-C/Cu/Cu_2O for the terminal alkyne homo-coupling reaction, as compared to WO_3/Cu_2O, offers compelling evidence supporting the Z-scheme migration mechanism within the WO_3/N-C/Cu/Cu_2O heterojunction. In addition, we have conducted experiments to prove the important influences of photo-generated hole and electron, and $\cdot O_2$ (Fig. S14). The cycle stability of the catalysts has been evaluated (Fig. 5d), and the WO_3/N-C/Cu/Cu_2O heterojunction demonstrates outstanding cycle stability with no obvious loss of photocatalytic efficiency and no changes in the structure and morphology after three cycles of photocatalytic reactions (Fig. S15). To further validate the high catalytic activity of WO_3/N-C/Cu/Cu_2O, we have conducted the photocatalytic oxidation of various alkynes substrates under identical conditions. As shown in Fig. 5e, the yields of the corresponding target products ranged from 80% to 99%, confirming that the Z-scheme WO_3/N-C/Cu/Cu_2O heterojunction is an exceptional photocatalyst under blue light (λ=450 nm).

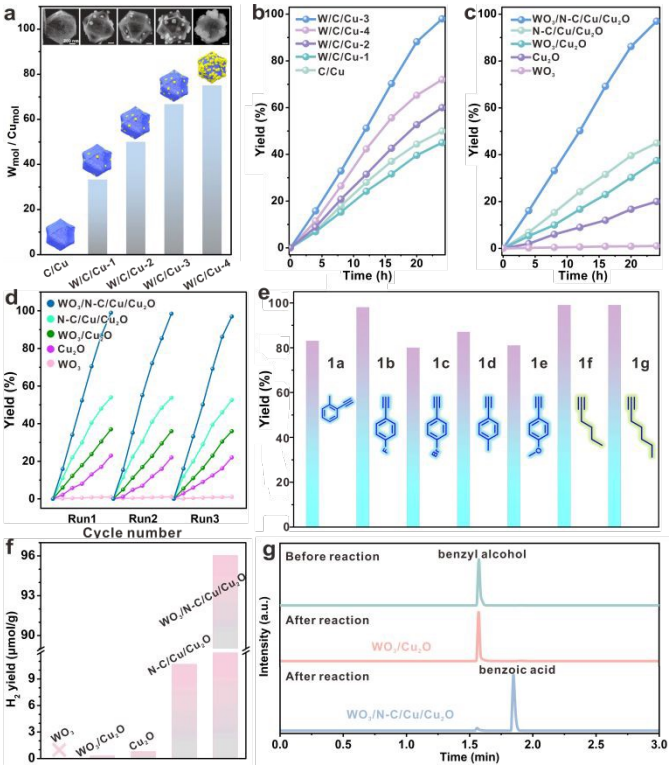

Fig. 5 (a) The histogram of different W/Cu contents and the corresponding SEM images, (b) the yield of homo-coupling of phenylacetylen by different W/Cu contents samples, (c) the yield of homo-coupling of phenylacetylen by WO_3/N-C/Cu/Cu_2O, N-C/Cu/Cu_2O, Cu_2O, WO_3/Cu_2O, and WO_3 samples, (d) stability test of the various photocatalysts for the homo-coupling of phenylacetylene, (e) performance of WO_3/N-C/Cu/Cu_2O in homo-coupling of various alkynes, (f) the photocatalytic hydrogen yields over WO_3/N-C/Cu/Cu_2O, N-C/Cu/Cu_2O, Cu_2O, WO_3/Cu_2O, and WO_3 samples with benzyl alcohol as the hole capturer, (g) the retention time of different aqueous solution (unreacted benzyl alcohol solution and reaction solutions with WO_3/Cu_2O and WO_3/N-C/Cu/Cu_2O as photocatalysts, respectively) detected by liquid chromatography.

To further confirm the Z-scheme mechanism of the WO_3/N-C/Cu/Cu_2O heterojunction and its influence on catalytic performance, the WO_3/N-C/Cu/Cu_2O heterojunction has been employed as catalyst for photocatalytic hydrogen production using benzyl alcohol as the hole capture. As illustrated in Fig. 5f, under irradiation of blue light, the hydrogen production efficiency of the five samples follows the order: WO_3/N-C/Cu/Cu_2O > N-C/Cu/Cu_2O > Cu_2O > WO_3/Cu_2O > WO_3.

Amongst, the CB potential of WO_3 is more positive than the H^+/H_2 potential (0 V vs. NHE), therefore WO_3 lacks the ability to photocatalyze hydrogen production. The hydrogen production rate of WO_3/N-C/Cu/Cu_2O is 9 times and 120 times higher than N-C/Cu/Cu_2O and Cu_2O, respectively, indicating that the constructed WO_3/N-C/Cu/Cu_2O heterojunction interface can significantly facilitate efficient migration and separation of photogenerated carriers. Moreover, the hydrogen production of WO_3/N-C/Cu/Cu_2O is 300 times greater than WO_3/Cu_2O, suggesting that the photogenerated electrons in WO_3/N-C/Cu/Cu_2O are predominantly accumulated in the CB of Cu_2O, thereby promoting the reduction reaction for hydrogen production. The reaction solutions after the photocatalysis over these five catalysts have been analyzed using liquid chromatography, and the results are presented in Fig. 5g and Fig. S16. With WO_3/Cu_2O, N-C/Cu/Cu_2O, and Cu_2O as photocatalysts, only unreacted benzyl alcohol can be detected, indicating that no conversion of benzyl alcohol to benzoic acid has occurred under these conditions. In contrast, in the reaction solution of WO_3/N-C/Cu/Cu_2O and WO_3, both the benzyl alcohol and benzoic acid have been observed. The benzoic acid can be produced via the oxidation of benzyl alcohol by ·OH or photogenerated holes. This observation can be attributed to the VB position of WO_3 (+2.62 V vs. NHE) being more positive than the redox potential of benzaldehyde/benzoic acid couple (+2.5 V vs. NHE).[49] These findings suggest that in the WO_3/N-C/Cu/Cu_2O system, photogenerated holes ultimately accumulate on the VB of WO_3 to participate in the oxidation reaction, providing another strong evidence for the preserved high redox potentials in the obtained Z-scheme WO_3/N-C/Cu/Cu_2O heterojunction.

To further verify the effective separation and migration of photogenerated carriers within the constructed Z-scheme WO_3/N-C/Cu/Cu_2O heterojunction, we have conducted measurements of photocurrent density and electrochemical impedance spectroscopy (EIS) for WO_3/N-C/Cu/Cu_2O, N-C/Cu/Cu_2O, WO_3/Cu_2O, Cu_2O, and WO_3 samples. As illustrated in Fig. S17a, the photocurrent densities of WO_3/N-C/Cu/Cu_2O are 2, 3, 5, and 5 times higher than N-C/Cu/Cu_2O, WO_3/Cu_2O, Cu_2O, and WO_3, respectively. This suggests that the formation of multiple interfaces does not undermine the positive promoting effect of the WO_3/N-C/Cu/Cu_2O heterojunction on the separation of photogenerated carriers. The order of EIS radius of these five samples (Fig. S17b) is WO_3/N-C/Cu/Cu_2O < N-C/Cu/Cu_2O < WO_3/Cu_2O < Cu_2O < WO_3. Generally, a smaller arc radius implies higher charge transfer efficiency. Therefore, WO_3/N-C/Cu/Cu_2O exhibits the highest charge transfer efficiency among these five samples. This further confirms that the WO_3/N-C/Cu/Cu_2O interface in the Z-scheme heterojunction we constructed is sufficiently robust, providing an efficient and smooth pathway for the migration and separation of photogenerated carriers.

Conclusions

In this work, a "post-deposition and pyrolysis" synthesis strategy has been employed to fabricate a Z-scheme WO_3/N-C/Cu/Cu_2O heterojunction featuring a tightly integrated interface. The XPS spectra analysis and work function calculation reveal the opposite directions of interfacial electron migration in WO_3/N-C/Cu/Cu_2O and WO_3/Cu_2O heterojunctions. These findings preliminarily demonstrate that the modified heterojunction interface can effectively overcome the mismatched work function of WO_3 and Cu_2O, control the direction of ground-state electron migration, thereby modulating the orientation of the built-in electric field at the interface. The results of EPR and photocatalytic tests have confirmed that the WO_3/N-C/Cu/Cu_2O heterojunction can preserve the energetic photogenerated holes of WO_3 and the photogenerated electrons of Cu_2O for participation in the redox reaction. The fs-TA spectroscopy elucidates the migration pathway of photogenerated carrier in the WO_3/N-C/Cu/Cu_2O heterojunction. Specifically, the photogenerated electrons from WO_3 recombine with the photogenerated holes of Cu_2O enriched on Cu through the mediation of the N-C layer, which is a typical Z-scheme charge transfer mechanism. This research not only introduces a novel concept in interface engineering for constructing efficient heterojunction photocatalysts but also provides a synthetic strategy for building effective and compact heterojunction interfaces.

Author contributions

The manuscript was written through contributions of all authors. All authors have given approval to the final version of the manuscript. In detailed, H. Gao, X. He, and J. Li contributed equally in the investigation and data curation, C. Qin supported the visualization, S. Zhi supported the data curation, L. Yang and J. Zhao contributed to the software, L. Sun, W. Zhan, and X. Han contributed to the conceptualization and writing.

Conflicts of interest

There are no conflicts to declare.

Data availability

The data supporting this article have been included as part of the Supplementary Information.

Acknowledgements

This work was supported by the Xuzhou Key Research and Development Program (Social Development) (No. KC23298), the National Natural Science Foundation of China (Grant No. 22271122), the Natural Science Foundation of the Jiangsu Higher Education Institutions of China (24KJA150003), Basic Research Program of Jiangsu (BK20253049). We thank Materials Characterization Center of East China Normal University for help with the measurement of femtosecond TA.

Notes and references

1 X. Sun, X. Zhang and Y. Xie, *Matter*, 2020, **2**, 842-861.
2 Z. Zhang, X. Chen, H. Zhang, W. Liu, W. Zhu and Y. Zhu, *Advanced Materials*, 2020, **32**, 1907746.
3 J.-R. Huang, W.-X. Shi, S.-Y. Xu, H. Luo, J. Zhang, T.-B. Lu and Z.-M. Zhang, *Advanced Materials*, 2024, **36**, 2306906.
4 Y.-J. Wang, X. Cheng, N.-N. Ma, W.-Y. Cheng, P. Zhang, F. Luo, W.-X. Shi, S. Yao, T.-B. Lu and Z.-M. Zhang, Angewandte Chemie International Edition, 2025, **64**, e202423204.
5 S. Zhao, S.-S. Shen, L. Han, B.-C. Tian, N. Li, W. Chen and X.-B. Li, *Rare Metals*, 2024, **43**, 4038-4055.
6 R. Chen, S. Pang, H. An, J. Zhu, S. Ye, Y. Gao, F. Fan and C. Li, *Nature Energy*, 2018, **3**, 655-663.
7 L. Pan, M. Ai, C. Huang, L. Yin, X. Liu, R. Zhang, S. Wang, Z. Jiang, X. Zhang, J.-J. Zou and W. Mi, *Nature Communications*, 2020, **11**, 418.
8 Z. Wang, Z. Lin, S. Shen, W. Zhong and S. Cao, *Chinese Journal of Catalysis*, 2021, **42**, 710-730.
9 J. Low, J. Yu, M. Jaroniec, S. Wageh and A. A. Al-Ghamdi, *Advanced Materials*, 2017, **29**, 1601694.
10 D. Zhao, Y. Wang, C.-L. Dong, Y.-C. Huang, J. Chen, F. Xue, S. Shen and L. Guo, *Nature Energy*, 2021, **6**, 388-397.
11 X. Chen, J. Wang, Y. Chai, Z. Zhang and Y. Zhu, *Advanced Materials*, 2021, **33**, 2007479.
12 J. Fu, J. Yu, C. Jiang and B. Cheng, *Advanced Energy Materials*, 2018, **8**, 1701503.
13 Q. Xu, L. Zhang, J. Yu, S. Wageh, A. A. Al-Ghamdi and M. Jaroniec, *Materials Today*, 2018, **21**, 1042-1063.
14 P. Zhou, J. Yu and M. Jaroniec, *Advanced Materials*, 2014, **26**, 4920-4935.
15 Y. Li, K. Chen, X. Wang, Z. Xiao, G. Liao, J. Wang, X. Li, Y. Tang, C. He and L. Li, *Chemosphere*, 2022, **308**, 136259.
16 G. Zhang and Y. Wang, *Polyoxometalates*, 2023, **2**, 9140020.
17 X. Li, Q. Liu, F. Deng, J. Huang, L. Han, C. He, Z. Chen, Y. Luo and Y. Zhu, *Applied Catalysis B-Environment and Energy*, 2022, **314**, 121502.
18 M. Zhang, Y. Mao, X. Bao, G. Zhai, D. Xiao, D. Liu, P. Wang, H. Cheng, Y. Liu, Z. Zheng, Y. Dai, Y. Fan, Z. Wang and B. Huang, *Angewandte Chemie-International Edition*, 2023, **62**, e202302919.
19 H. Zhao, L. Wang, G. Liu, Y. Liu, S. Zhang, L. Wang, X. Zheng, L. Zhou, J. Gao, J. Shi and Y. Jiang, *ACS Catalysis*, 2023, **13**, 6619-6629.
20 P. Xia, S. Cao, B. Zhu, M. Liu, M. Shi, J. Yu and Y. Zhang, *Angewandte Chemie-International Edition*, 2020, **59**, 5218-5225.
21 J. Du, I. Ahmad, I. M. Ashraf, F. B. M. Ahmed, A. Aslam, I. Ali, A. Mohammad and M. A. Khasawneh, *International Journal of Hydrogen Energy*, 2025, **100**, 1361-1384.
22 W. Wang, S. Mei, H. Jiang, L. Wang, H. Tang and Q. Liu, *Chinese Journal of Catalysis*, 2023, **55**, 137-158.
23 Y. Zhang, Z. Jin, D. Liu, Z. Tan, B. B. Mamba, A. T. Kuvarega and J. Gui, *ACS Applied Nano Materials*, 2022, **5**, 5448-5458.
24 S. Wu, X. Yu, J. Zhang, Y. Zhang, Y. Zhu and M. Zhu, *Chemical Engineering Journal*, 2021, **411**, 128555.
25 X. Li, Y. Wan, F. Deng, Y. Zhou, P. Chen, F. Dong and J. Jiang, *Chinese Chemical Letters*, 2025, **36**, 111418.
26 L. Zhang, J. Zhang, H. Yu and J. Yu, *Advanced Materials*, 2022, **34**, 2107668.
27 Q. Xu, L. Zhang, B. Cheng, J. Fan and J. Yu, *Chem*, 2020, **6**, 1543-1559.
28 J. Fu, Q. Xu, J. Low, C. Jiang and J. Yu, *Applied Catalysis B-Environmental*, 2019, **243**, 556-565.
29 Q. Xu, S. Wageh, A. A. Al-Ghamdi and X. Li, *Journal of Materials Science & Technology*, 2022, **124**, 171-173.
30 J. Wang, Q. Zhang, F. Deng, X. Luo and D. D. Dionysiou, *Chemical Engineering Journal*, 2020, **379**, 122264.
31 P. Shandilya, S. Sambyal, R. Sharma, P. Mandyal and B. Fang, *Journal of Hazardous Materials*, 2022, **428**, 128218.
32 H. Gong, Y. Zhang, Y. Cao, M. Luo, Z. Feng, W. Yang, K. Liu, H. Cao and H. Yan, *Applied Catalysis B-Environmental*, 2018, **237**, 309-317.
33 Q. Wei, Y. Wang, H. Qin, J. Wu, Y. Lu, H. Chi, F. Yang, B. Zhou, H. Yu and J. Liu, *Applied Catalysis B-Environmental*, 2018, **227**, 132-144.
34 R. Camposeco, S. Castillo, V. Rodriguez-Gonzalez, M. Hinojosa-Reyes, M. I. Medina-Alvares and I. Mejia-Centeno, *Journal of Photochemistry and Photobiology a-Chemistry*, 2018, **353**, 114-121.
35 S. J. Hong, S. Lee, J. S. Jang and J. S. Lee, *Energy & Environmental Science*, 2011, **4**, 1781-1787.
36 J. Jin, J. Yu, D. Guo, C. Cui and W. Ho, *Small*, 2015, **11**, 5262-5271.
37 T. Fukumura, E. Sambandan and H. Yamashita, *Materials Research Bulletin*, 2017, **94**, 493-499.
38 S. Chen, Y. Hu, S. Meng and X. Fu, *Applied Catalysis B-Environment and Energy*, 2014, **150**, 564-573.
39 L. Zhang, Q. Shen, F. Huang, L. Jiang, J. Liu, J. Sheng, Y. Li and H. Yang, *Applied Surface Science*, 2023, **608**, 155064.
40 X. Li, B. Kang, F. Dong, Z. Zhang, X. Luo, L. Han, J. Huang, Z. Feng, Z. Chen, J. Xu, B. Peng and Z. L. Wang, *Nano Energy*, 2021, **81**, 105671.
41 C. Kim, K. M. Cho, A. Al-Saggaf, I. Gereige and H.-T. Jung, *ACS Catalysis*, 2018, **8**, 4170-4177.
42 H. Long, M. Zhao, T. Ma, Z. Lang, S. Zhang and C. Lei, *Materials Today Communications*, 2024, **41**, 110871.
43 J. He, D. W. Shao, L. C. Zheng, L. J. Zheng, D. Q. Feng, J. P. Xu, X. H. Zhang, W. C. Wang, W. H. Wang, F. Lu, H. Dong, Y. H. Cheng, H. Liu and R. K. Zheng, *Applied Catalysis B-Environmental*, 2017, **203**, 917-926.
44 K. Sun, X. Zhao, Y. Zhang, D. Wu, X. Zhou, F. Xie, Z. Tang and X. Wang, *Materials Chemistry and Physics*, 2020, **251**, 123172.
45 S. S. Y. Chui, S. M. F. Lo, J. P. H. Charmant, A. G. Orpen and I. D. Williams, *Science*, 1999, **283**, 1148-1150.
46 D. Zu, Y. Ying, Q. Wei, P. Xiong, M. S. Ahmed, Z. Lin, M. M.-J. Li, M. Li, Z. Xu, G. Chen, L. Bai, S. She, Y. H. Tsang and H. Huang, *Angewandte Chemie-International Edition*, 2024, **63**, e202405756.
47 X. Ruan, D. Meng, C. Huang, M. Xu, D. Jiao, H. Cheng, Y. Cui, Z. Li, K. Ba, T. Xie, L. Zhang, W. Zhang, J. Leng, S. Jin, S. K. Ravi, Z. Jiang, W. Zheng, X. Cui and J. Yu, *Advanced Materials*, 2024, **36**, 2309199.
48 S. Cao, B. Shen, T. Tong, J. Fu and J. Yu, *Advanced Functional Materials*, 2018, **28**, 1800136.
49 F. M. Pesci, A. J. Cowan, B. D. Alexander, J. R. Durrant and D. R. Klug, *Journal of Physical Chemistry Letters*, 2011, **2**, 1900-1903.
50 X. Han, X. He, L. Sun, X. Han, W. Zhan, J. Xu, X. Wang and J. Chen, *ACS Catalysis*, 2018, **8**, 3348-3356.
51 S. E. Allen, R. R. Walvoord, R. Padilla-Salinas and M. C. Kozlowski, *Chemical Reviews*, 2013, **113**, 6234-6458.
52 Z.-H. Zhang, X.-Y. Dong, X.-Y. Du, Q.-S. Gu, Z.-L. Li and X.-Y. Liu, *Nature Communications*, 2019, **10**, 5689.
53 X.-Y. Dong, J.-T. Cheng, Y.-F. Zhang, Z.-L. Li, T.-Y. Zhan, J.-J. Chen, F.-L. Wang, N.-Y. Yang, L. Ye, Q.-S. Gu and X.-Y. Liu, *Journal of the American Chemical Society*, 2020, **142**, 9501-9509.
54 K. Kamata, S. Yamaguchi, M. Kotani, K. Yamaguchi and N. Mizuno, *Angewandte Chemie-International Edition*, 2008, **47**, 2407-2410.
55 Y. Zhu and Y. Shi, *Organic & Biomolecular Chemistry*, 2013, **11**, 7451-7454.
56 W. Lu, X. Yu and M. Bao, *Green Chemistry*, 2023, **25**, 5123-5127.
57 X. Yan, T. Xu, W. Zhan, Y. Yang, Y. Yu, J. Yi, X. He, L. Yang, J. Zhao, L. Sun and X. Han, *Nano Research*, 2024, **17**, 6895-6902.

58 H. G. Roth, N. A. Romero and D. A. Nicewicz, *Synlett*, 2016, **27**, 714-723.

View Article Online
DOI: 10.1039/D5SC05362E

View Article Online
DOI: 10.1039/D5SC05362E

Data availability statements

The data supporting this article have been included as part of the Supplementary Information.